AIAA JOURNAL
Vol. 48, No. 6, June 2010

Numerical Investigation of Transverse Hydrogen Jet into Supersonic Crossflow Using Detached-Eddy Simulation

Su-Hee Won* and In-Seuck Jeung†
Seoul National University, Seoul 151-742, Republic of Korea
and
Bernard Parent‡ and Jeong-Yeol Choi§
Pusan National University, Busan 609-735, Republic of Korea

DOI: 10.2514/1.41165

A three-dimensional unsteady reacting flowfield that is generated by transverse hydrogen injection into a supersonic mainstream is numerically investigated using detached-eddy simulation and a finite-rate chemistry model. Grid refinement with the grid-convergence-index concept is applied to the instantaneous flowfield for assessing the grid resolution and solution convergence. Validation is performed for the jet penetration height, and the predicted result is in good agreement with experimental trends. The results indicate that jet vortical structures are generated as the interacting counter-rotating vortices become alternately detached in the upstream recirculation region. Although the numerical OH distribution reproduces the experimental OH–planar-laser-induced fluorescence well, there are some disparities in the ignition delay times due to the restricted availability of experimental and numerical data. The effects of the turbulence model on combustion are identified by a comparative analysis of the Reynolds-averaged Navier–Stokes and detached-eddy simulation approaches. Their effects are quantified by the production of H_2O, which is the primary species of hydrogen combustion.

Nomenclature

C_{DES}, $C^{k\text{-}\varepsilon}_{\mathrm{DES}}$, $C^{k\text{-}\omega}_{\mathrm{DES}}$	=	closure coefficients in the detached-eddy simulation model
D^k_{RANS}, D^k_{DES}	=	dissipation of turbulent kinetic energy
d	=	injector diameter
F_1	=	switching function for Menter's shear-stress-transport model
J	=	jet-to-freestream momentum flux ratio
k	=	turbulent kinetic energy
L	=	distance of the injection port from the flat plate's leading edge
l_{RANS}, l_{DES}	=	turbulent length scale
M	=	Mach number
P_k	=	production of turbulent kinetic energy
p	=	static pressure
Re	=	Reynolds number
T	=	static temperature
t	=	time
x, y, z	=	Cartesian coordinates
y^+	=	nondimensional wall distance
β, γ, $\sigma_{\omega1}$, $\sigma_{\omega2}$	=	closure coefficients in the specific dissipation rate equation
β^*, σ_k	=	closure coefficients in the turbulent-kinetic-energy equation
Δ	=	characteristic length based on the maximum grid-size/difference operator
δ	=	boundary-layer thickness at the injector port
ε	=	dissipation rate
μ, μ_t	=	molecular and turbulent dynamic viscosity
ρ	=	density
τ	=	ignition delay time
φ	=	equivalence ratio
ω	=	specific dissipation rate
ω_x, ω_y, ω_z, ω_m	=	x, y, and z vortical components and vorticity magnitude

Subscripts

exp.	=	property based on experimentation
j	=	injector exit value
mix	=	property of the mixing layer
nu.	=	property based on numerical simulation
2	=	property behind the bow shock
∞	=	freestream value

Received 22 September 2008; revision received 4 February 2010; accepted for publication 14 February 2010.

*Graduate Student, School of Mechanical and Aerospace Engineering. Student Member AIAA.

†Professor, Department of Aerospace Engineering, Institute of Advanced Aerospace Technology. Associate Fellow AIAA.

‡Assistant Professor, Department of Aerospace Engineering. Member AIAA.

§Professor, Department of Aerospace Engineering; aerochoi@pusan.ac.kr. Senior Member AIAA (Corresponding Author).

I. Introduction

ONE of the critical issues for a scramjet combustor is the realization of efficient fuel–air mixing and combustion within a short flow residence time. The flow residence time associated with hypersonic flight speeds is typically of the order of milliseconds; therefore, fuel should be mixed with air and burned completely within such a limited time span to reduce the combustor length and weight. A number of research studies have been conducted on this topic. Various injection concepts have been suggested for scramjet combustor configurations to overcome the limited flow residence time. Transverse fuel injection through a wall orifice is one of the conventional and reliable methods that enable rapid fuel–air mixing and high jet penetration into supersonic crossflow.

The configuration of transverse fuel injection is simple, but the generated flow structures are rather complicated, as shown in Fig. 1. The leaving jet expands rapidly and blocks the supersonic crossflow, causing a three-dimensional bow shock ahead of the injector. The bow shock causes separation of the upstream wall boundary layer, where the fuel is subsonically mixed with the air. This region of subsonic mixing is important in transverse injection flowfields, due to its flame-holding capability inside a supersonic combustor. Furthermore, as the fuel jet interacts with the supersonic crossflow,

various coherent structures are generated that have been considered important because of their roles in the enhancement of fuel–air mixing. These coherent structures are generally classified into four types [1,2]. The first dominant vortex structures are the shear-layer vortices that develop large-scale eddy structures along the jet-shear-layer periphery. These eddy structures enhance near-field mixing by entraining freestream fluid into the jet shear layer and increasing the interfacial area between the unmixed fluids. Second, the streamwise counter-rotating vortex pair contributes to the enhancement of mixing by causing the freestream fluid to be engulfed by the jet core. The third vortex system is the horseshoe vortex that wraps around the jet column and flows downstream along the wall. Finally, the wake vortices identified through an incompressible experiment originate from the wall boundary layer, but their roles in the supersonic mixing process remain uncertain. Figure 1 illustrates the shock and coherent structures for the supersonic jet in crossflow, as have been revealed in previous publications [2–4].

On the other hand, several recent experimental studies have revealed interesting features of unsteady flow. Papamoschou and Hubbard [5] and Gruber et al. [4] reported fluid dynamic instabilities in transverse injection flowfields. Ben-Yakar et al. [2] observed essentially the same jet instability in their supersonic combustion experiments and achieved temporally resolved visualization with a high-speed camera for both nonreactive and reactive flowfields. However, the difficulties in measuring complex high-speed unsteady flowfields restrict the availability of experimental data, which are as yet insufficient to account for the underlying mechanisms. Therefore, numerical approaches are an attractive alternative for supplementing insights into unsteady features for supersonic mixing and combustion flowfields.

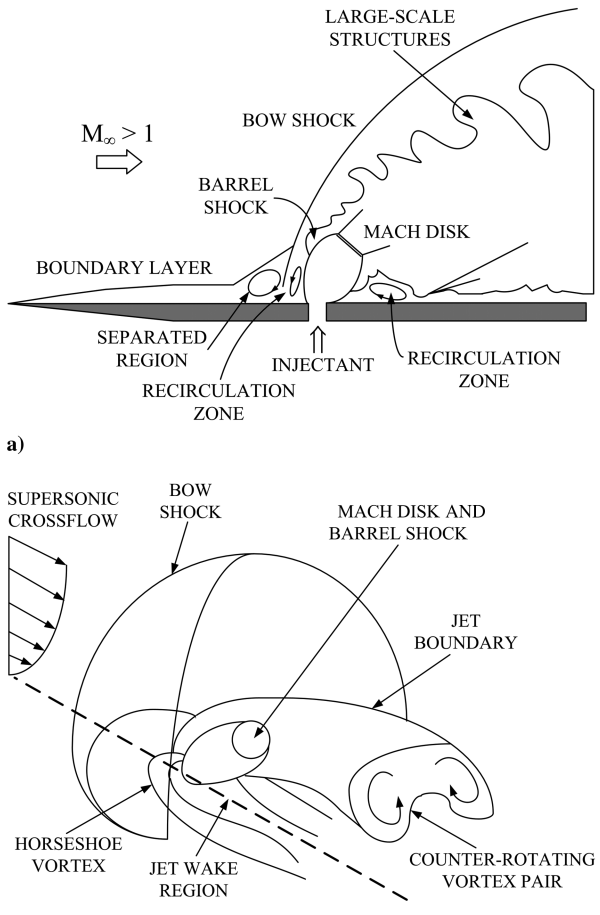

Fig. 1 Schematic of an underexpanded transverse injection into a supersonic crossflow [2]: a) instantaneous side view and b) average perspective view.

Reynolds-averaged Navier–Stokes (RANS) turbulent models are obviously insufficient for capturing the features of unsteady flow, owing to their intrinsic dissipative and time-averaging characteristics [6,7]. More recently, several attempts have been undertaken with regard to detached-eddy simulation (DES) and large-eddy simulation (LES) methods to overcome the conventional limitations of the RANS models. Peterson et al. [8,9] revealed large-scale eddy structures through the DES approach and discussed the capability of DES for capturing the features of unsteady turbulent flow in transverse injection flowfields. Kawai and Lele [10] and Boles et al. [11] performed LES and provided some insight into supersonic jet mixing processes using instantaneous flow structures. Although improved results were achieved in previous studies, the computational applications were restricted to nonreactive or relatively low Reynolds-number flows, which are discrepant with the case of a realistic scramjet combustor environment.

The unsteady nature of turbulent reacting flowfields was studied numerically by Choi et al. for a scramjet configuration with transverse fuel injection and a cavity flame holder [12,13]. They showed that the unsteady flow and flame dynamics were related to intrinsic instability as well as cavity-driven instability. Although they showed that the capture of unsteady eddy motion is crucial to the accurate prediction of combustor performance, their study was limited to two-dimensional simulation, which is insufficient to explain the characteristics of real three-dimensional flow. Von Lavante et al. performed a three-dimensional calculation using LES and finite-rate chemistry [14]. They showed the unsteady features of a three-dimensional jet in crossflow, but their focus was on describing the experimentally observed flow features and the difference between the two- and three-dimensional numerical results. The underlying physics of the turbulent reacting flow were not discussed in detail.

The present study seeks to simulate the complex unsteady flowfield of a real supersonic combustor environment using the DES approach. Although LES entails high computational cost for the high Reynolds-number flows that are associated with a real supersonic combustor environment, DES is a less-expensive hybrid method that operates at a traditional RANS mode in the attached boundary layer and at a LES mode in the rest of the flow. The hydrogen-injection case of Ben-Yakar et al.'s experiment [2] is selected as the computational configuration, because their experiments had been performed in a real supersonic combustor environment for a flight Mach number of 10. The consecutive schlieren images and planar laser-induced fluorescence of OH radicals (OH–PLIF) using a high-speed framing camera also provide flexibility in comparing the computational results and the experimental data. The main objective of the current study is to gain further insight into the physics of turbulent mixing and reacting flows in supersonic transverse injection flowfields. Through systematic comparative analyses, the temporal evolution of coherent structures is investigated to ascertain the convection characteristics and underlying mechanism of the formation of such structures. The unsteady simulation with finite-rate chemistry is compared with experimental data for examining the supersonic turbulent reacting flow physics in a realistic scramjet combustor environment.

II. Numerical Approach

A. Governing Equations and Numerical Methods

The three-dimensional turbulent reacting flowfields are described through the conservation equations for a multispecies chemically reactive system. The coupled governing equations of species conservation, fluid dynamics, and turbulent transport are expressed in the following conservative vector form,

$$\frac{\partial \boldsymbol{Q}}{\partial t} + \frac{\partial \boldsymbol{E}}{\partial x} + \frac{\partial \boldsymbol{F}}{\partial y} + \frac{\partial \boldsymbol{G}}{\partial z} = \frac{\partial \boldsymbol{E}_v}{\partial x} + \frac{\partial \boldsymbol{F}_v}{\partial y} + \frac{\partial \boldsymbol{G}_v}{\partial z} + \boldsymbol{W} \qquad (1)$$

where the conservative variable vector $\boldsymbol{Q}$, the convective flux vectors $\boldsymbol{E}$, $\boldsymbol{F}$, and $\boldsymbol{G}$, the viscous flux vectors $\boldsymbol{E}_v$, $\boldsymbol{F}_v$, and $\boldsymbol{G}_v$, and the reaction source term $\boldsymbol{W}$ are defined in the previous paper [15].

The finite-volume approach is used for the spatial discretization of the governing equations. The viscous terms are expressed by the central difference method, and the convective terms are expressed as the differences in the numerical fluxes at the cell interface. The numerical fluxes containing artificial dissipation are formulated using Roe's flux difference splitting method. The MUSCL (monotone upstream-centered schemes for conservation laws) scheme is used for the extrapolation of primitive variables at the cell interface. In addition, the Chakravarthy and Osher limiter function is used to overcome the dispersion error that is introduced by the third-order extrapolation and to preserve the total-variation-diminishing property. For an analysis of unsteady supersonic reacting flow, a fully implicit, lower–upper symmetric Gauss–Seidel method is used with second-order accuracy. A Newton subiteration method is applied to reduce the error in temporal discretization and ensure second-order time accuracy and stability, thereby allowing a large time step. Details of the governing equations and the numerical formulation are described in previous studies [12,13,16].

B. Turbulence and Thermochemical Model

In the present study, the DES approach is adopted to capture large-scale turbulent structures in high Reynolds-number flowfields. The DES, first proposed by Spalart et al. [17], is a hybrid method for combining the advantages of RANS models in terms of simulation costs and the ability of LES to capture unsteady flow structures. This model was originally based on the Spalart–Allmaras one-equation RANS turbulence model; a modified version of Menter's shear stress transport (SST) model was introduced by Strelets [18]. The classical formulation of Menter's SST model is given by [19],

$$\frac{\mathrm{D}}{\mathrm{D}t}(\rho k) = P_k - \beta^* \rho k\omega + \frac{\partial}{\partial x_j}\left[(\mu + \sigma_k \mu_t)\frac{\partial k}{\partial x_j}\right] \tag{2}$$

$$\frac{\mathrm{D}}{\mathrm{D}t}(\rho\omega) = \frac{\rho\gamma}{\mu_t}P_k - \beta\rho\omega^2 + \frac{\partial}{\partial x_j}\left[(\mu + \sigma_{\omega 1}\mu_t)\frac{\partial \omega}{\partial x_j}\right] + 2(1-F_1)\rho\sigma_{\omega 2}\frac{1}{\omega}\frac{\partial k}{\partial x_j}\frac{\partial \omega}{\partial x_j} \tag{3}$$

where the RANS-length scale (l_{RANS}) is replaced by the DES-length scale (l_{DES}) in the dissipative term of the k-transport equation. The dissipative terms and related turbulent length scales are defined as

$$D^k_{\mathrm{RANS}} = \beta^* \rho k\omega = \rho k^{3/2}/l_{\mathrm{RANS}}; \qquad l_{\mathrm{RANS}} = k^{1/2}/(\beta^*\omega) \tag{4}$$

$$D^k_{\mathrm{DES}} = \rho k^{3/2}/l_{\mathrm{DES}}; \qquad l_{\mathrm{DES}} = \min(l_{\mathrm{RANS}}, C_{\mathrm{DES}}\Delta) \tag{5}$$

where $\Delta[=\max(\Delta x, \Delta y, \Delta z)]$ is based on the largest dimension of the local grid cell. In the boundary layer, the model acts in the RANS mode but switches to the LES mode in detached regions. Because Menter's SST model [19] is based on the blending of the k-ε and k-ω turbulence models, C_{DES} is calibrated for both models and blended by the blending function F_1; that is,

$$C_{\mathrm{DES}} = (1-F_1)C^{k\text{-}\varepsilon}_{\mathrm{DES}} + F_1 C^{k\text{-}\omega}_{\mathrm{DES}}$$

The recommended constants, $C^{k\text{-}\varepsilon}_{\mathrm{DES}} = 0.61$ and $C^{k\text{-}\omega}_{\mathrm{DES}} = 0.78$, are used for turbulence closure in the current study [18].

The closure problem is important for the interaction between turbulence and chemistry in supersonic combustion. Because combustion is a multiscale process, Peters recommended the use of turbulent combustion modeling based on this process [e.g., probability density function (PDF)-based models] [20]. Great progress has been made in modeling nonpremixed turbulent combustion at lower speeds (e.g., through flamelet theory and PDF methods). Although some attempts have been made to solve for supersonic combustion processes, the improvements have been relatively insignificant in comparison with the results obtained from laminar chemistry and experimental data, as discussed by Möbus et al. [21], in spite of the complexity in modeling turbulence-chemistry interactions. A careful review of existing results, such as the one made by Norris and Edwards [22], suggests that solution accuracy seems to be dependent on the grid resolution, as in a LES study of supersonic turbulent combustion. Another important issue is the degree of detail in chemical kinetics for analyzing ignition and flame stabilization. A carefully validated case for supersonic combustion shows that a single-step mechanism results in premature ignition and a more stable flame when compared with a multistep mechanism [23]. Therefore, a detailed chemistry model is needed to more accurately describe high-speed turbulent diffusion flames. Based on the knowledge acquired in previous studies, the effect of turbulence on the chemical reaction rate is not considered in the present work, but detailed kinetics are considered to account for the ignition characteristics.

The present analysis employs the GRI-Mech 3.0 chemical kinetics mechanism for hydrogen–air combustion [24]. The GRI-Mech mechanism was originally developed for methane combustion. However, the hydrogen subset has also been validated for the ignition delay time of stoichiometric hydrogen–air mixtures [24] and has been used successfully for supersonic combustion simulations [12,13]. The mechanism consists of eight reactive species (H, H_2. O, O_2. H_2O, OH, H_2O_2, and HO_2) and 25 reaction steps. Nitrogen is assumed as an inert gas, because its oxidation process has only a minor effect on flame evolution in a combustor. The thermodynamic data and transport properties are taken from an earlier two-dimensional code [12] and partially updated with the most recent data available. The turbulent Prandtl and Schmidt numbers are assumed to be 0.9 for evaluating the turbulent thermal conductivity and mass diffusivity, respectively.

III. Verification and Validation

A. Computational Conditions

The experimental configuration consists of a flat plate and an attached high-speed solenoid valve that allows constant rates of injection flow during the duration of the test. A sonic jet of hydrogen is vertically injected into the external flow of the Mach number, $M_\infty = 3.38$, through a port of diameter, $d_j = 2$ mm. This jet-exit condition corresponds to the jet-to-freestream momentum flux ratio J of 1.4. The injection port is located at $L_\infty = 50$ mm downstream from the flat plate's leading edge, and the freestream boundary-layer thickness is approximately $\delta_\infty = 0.75$ mm ahead of the injection port. The details of the freestream and jet-exit properties are summarized in Table 1.

In the present numerical study, the three-dimensional computational domain is restricted to a finite region of the experimental configuration due to computational costs. As shown in Fig. 2a, the domain ranges from $5d_j$ upstream to $11d_j$ downstream of the fuel injector in the streamwise direction. For the spanwise and wall-normal directions, $12d_j$ and $10d_j$, respectively, are considered for the computational domain. A two-dimensional preliminary calculation is performed for the forward experimental configuration from the plate's leading edge to $20d_j$. The output is used as the inflow condition for a three-dimensional calculation in order to decrease the computational time. A region of focus with an evenly spaced grid is crucial for capturing large-eddy structures in DES. The present study distributes the region of focus around the jet exit, where the initial unsteady coherent structures are expected to develop.

All the dependent variables are specified from the preliminary two-dimensional output in the upstream boundary of the

Table 1 Supersonic crossflow and jet-exit flow conditions [2]

Supersonic crossflow		Injector exit (H_2)	
M_∞	3.38 ± 0.04	M_j	1
T_∞, K	1290	T_j, K	246
p_∞, kPa	32.4	p_j, kPa	490
L_∞, mm	50	d_j, mm	2
δ_∞, mm	0.75	J	1.4 ± 0.1
Re_∞	2.2×10^5	Re_{dj}	1.5×10^5

computational domain. The upper boundary is sufficiently far from the bottom plate, such that the shock waves generated in the interior pass out of the flowfield at the downstream boundary. Therefore, freestream conditions prevail at the top of the domain. A simple second-order extrapolation from the interior is used for the downstream boundary. The no-slip adiabatic condition is imposed at the wall, except over the injector exit. Uniform sonic injection is assumed at the injector boundary with the k and ω values recommended by Menter [19].

To examine the effects of grid resolution, three different sets of computational grids are generated. The grid levels 1, 2, and 3 correspond to coarse, medium, and fine grids, respectively. The refinement factor is selected to be about 1.5 in the x, y, and z directions to avoid excessive computational cost and determine the discretization error, using the grid convergence index (GCI). GCI, as suggested by Roache [25,26], is a methodology for the uniform reporting of grid-refinement studies and provides an error band on how far the solution is from the asymptotic value. The detailed procedure has been described in an earlier paper [15]. The grid points are clustered toward the wall to ensure that the first grid point away from the wall satisfies $y^+ < 1$ for the prediction of an attached RANS boundary layer. This applies to all possible levels for the grid system. A preliminary calculation under no injection shows good agreement to within 2% with respect to the boundary-layer thickness at the injection location. Figure 2b is the generated overall grid; every third grid point is presented in the figure. The number of grid points used in the current simulation and the physical dimensions of the computational domain are summarized in Table 2.

B. Verification for the Instantaneous Flowfield

As mentioned earlier, three different sets of grid points are generated and applied for simulations of an unsteady transverse jet in crossflow. The calculations are performed under the same flow

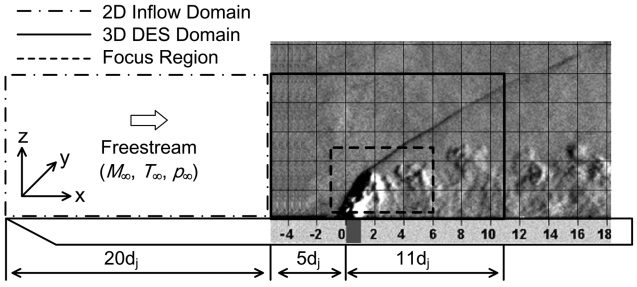

a)

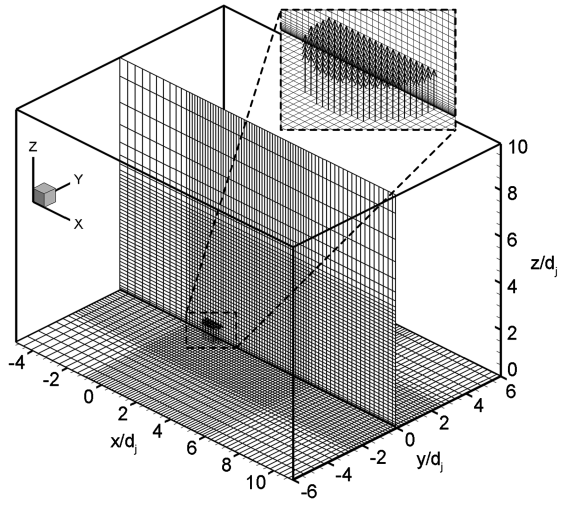

b)

Fig. 2 Computational domain and grid system: a) experimental configuration and computational domain and b) overall grid system (every third grid point).

Table 2 Number of grid points according to the resolution level

Grid	$x \times y \times z = 32 \times 24 \times 20$ mm
Level 1	$158 \times 98 \times 94 = 1,455,496$
Level 2	$234 \times 150 \times 138 = 4,843,800$
Level 3	$354 \times 222 \times 206 = 16,189,128$

conditions, except for the grid resolution. The resultant images are taken at the same physical time. Figure 3, as part of the results on grid refinement, describes the hydrogen-mass-fraction distribution around the injector. The flowfield of level 1, as shown in Fig. 3a, cannot capture the instantaneous large-eddy structures and converges to a steady state. However, the resultant images of levels 2 and 3, as shown in Figs. 3b and 3c, clearly show that the unsteady turbulent eddy structures and the overall flow structures are very similar to each other.

For a quantitative assessment of the grid quality, the temporal variations in the wall pressure are compared in Fig. 4. In the pressure-time history, a total of 17 probing points are considered from $x/d_j = -5$ to 11; only two results of probing ($x/d_j = 0$ and 5) are selected for convenience in the present assessment. The selected probing points are believed to collectively represent the characteristics of the flowfields upstream and downstream of the injector. Although the temporal history of the pressure at $x/d_j = 0$ shows very periodic behavior with high amplitude, the other pressure history at $x/d_j = 5$ shows somewhat anharmonic characteristics with relatively low amplitude. These anharmonic behaviors in the pressure-time history may stem from the complicated flow characteristics that are associated with the coherent structures present in the jet downstream. Although some differences exist in the pressure-time history according to the grid resolution, it is difficult to directly compare the respective histories. For further explicit expression of the characteristics of unsteady flow, the frequency spectrum of each pressure-time history is obtained using fast Fourier transforms (FFTs). The time period from 30 to 100 μs is considered in FFT analysis to exclude transient effects at the initial phase. The sampling range of 70 μs is rather short but reasonable for FFT analysis when the plate length and incoming flow velocity are considered.

As the grid is refined, the converged primary and secondary frequencies are observed in the frequency spectra, regardless of the position of probing. For example, the primary frequencies at $x/d_j = 0$ and 5 are 185.7 kHz in the coarse grid of level 1, whereas the primary frequencies of levels 2 and 3 are 198.9 kHz. Similar trends are observed in the secondary frequencies. By using the GCI concept on the basis of the frequency spectra, the calculated error bands indicate that the exact primary and secondary frequencies have been attained at $x/d_j = 0$ and 5. On the other hand, the amplitude analysis

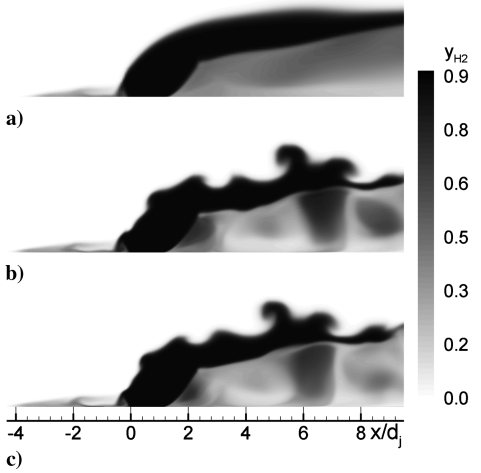

Fig. 3 Instantaneous images of the hydrogen mass fraction according to the grid resolution: a) level 1, b) level 2, and c) level 3.

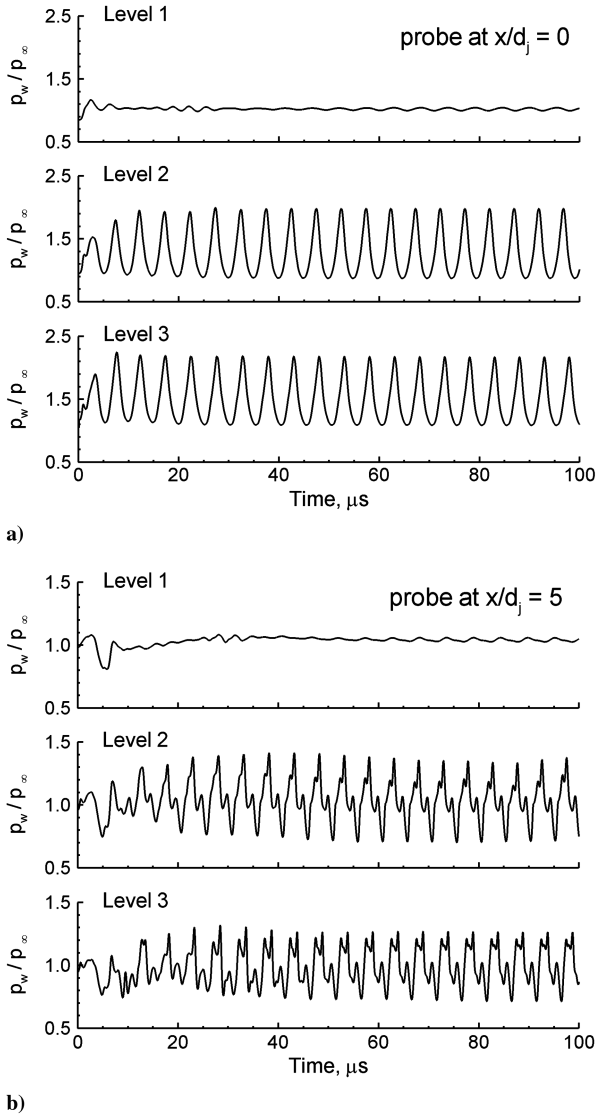

Fig. 4 Pressure-time history at the bottom wall: a) probe at $x/d_j = 0$ and b) probe at $x/d_j = 5$.

yields slightly different results. Although the primary amplitudes at $x/d_j = 0$ and 5 show converged results with a maximum error band of 2.60%, the secondary amplitude at $x/d_j = 5$ reveals a relatively large error band of 151.08%. This large error seems to arise from the amplitude contamination that is associated with complicated flow structures in the jet downstream and implies that the level 2 grid is still insufficient for resolving small turbulent structures. Tables 3 and 4 summarize the detailed GCI results for the present instantaneous flowfield.

In summary, the grid of level 1 is essentially insufficient for resolving the characteristics of unsteady flow. Although the level 2 grid fails to exactly predict the secondary amplitude at $x/d_j = 5$, it generally provides reasonable results with an acceptable computational cost when compared with the level 3 grid. From the results on grid refinement, the level 2 grid is considered for the present calculation.

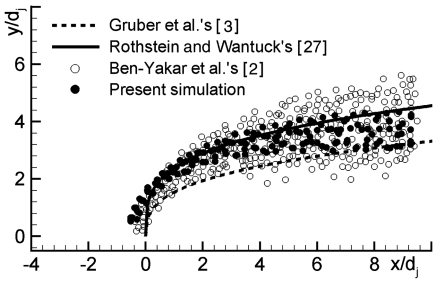

Fig. 5 Jet penetration and bandwidth of the transverse jet in crossflow.

C. Validation for the Jet Penetration Height

The jet penetration height is often used as the representative value to characterize the transverse jet in crossflow, because it is important for enhancing fuel–air mixing and avoiding wall heating in a scramjet combustor. The penetration height is also adequate for the validation and assessment of numerical results, which yield clear comparative data relatively easily. Therefore, the penetration data are presented in Fig. 5 to assess the numerical credibility and characterize the present jet in crossflow by comparison with the results of previous experimental studies.

A power-law fit for the penetration height has been proposed by various authors, and one of the most recent results has been suggested by Gruber et al. [3] through comprehensive experiments. In their experiments, the Mie scattering from ice particles was used to define the jet penetration where the jet concentration was about 10% at the boundary of the trajectory. Their power-law fit for circular injection is expressed in the form:

$$\frac{y}{d_j J} = 1.23\left(\frac{x}{d_j J}\right)^{1/3} \tag{6}$$

Another empirical correlation was suggested by Rothstein and Wantuck [27], who used OH–PLIF to visualize the jet penetration trajectory. Their experimental conditions were similar to Ben-Yakar et al.'s case [2], in which the underexpanded hydrogen jet was injected into a high-temperature air crossflow. The power-law fit based on OH–PLIF visualization is expressed in the following form:

$$\frac{y}{d_j J} = \frac{2.173}{J^{0.443}}\left(\frac{x}{d_j J}\right)^{0.821} \tag{7}$$

Ben-Yakar et al. [2] presented data on the jet penetration and bandwidth (i.e., the visible thickness of the jet shear layer) by measuring the visually observable outer edge of the jet from eight consecutive schlieren images. In their measurements, the visual jet penetration in the schlieren images corresponded to 1% of the jet concentration. In the same manner, data on the numerical penetration and bandwidth were extracted from 10 consecutive images and are presented in Fig. 5 to quantify the penetration properties.

The penetration data agree with the trend of increasing transverse penetration with the distance. However, differences in specific values are clearly observed depending on individual experiments. For example, at $8d_j$ downstream of the injection port, the penetration

Table 3 Primary GCI for instantaneous flowfields

	Primary frequency, kHz		Primary amplitude, p_w/p_∞	
Grid	$x/d_j = 0$	$x/d_j = 5$	$x/d_j = 0$	$x/d_j = 5$
Level 1	185.7	185.7	1.93×10^{-2}	1.08×10^{-2}
Level 2	198.9	198.9	4.62×10^{-1}	1.80×10^{-1}
Level 3	198.9	198.9	4.85×10^{-1}	1.58×10^{-1}
GCI_{23}	Exact	Exact	0.32%	2.60%

Table 4 Secondary GCI for instantaneous flowfields

	Secondary frequency, kHz		Secondary amplitude, p_w/p_∞	
Grid	$x/d_j = 0$	$x/d_j = 5$	$x/d_j = 0$	$x/d_j = 5$
Level 1	371.3	371.3	1.58×10^{-3}	2.30×10^{-3}
Level 2	397.8	397.8	1.05×10^{-1}	5.08×10^{-2}
Level 3	397.8	397.8	1.26×10^{-1}	8.69×10^{-2}
GCI_{23}	Exact	Exact	5.35%	151.08%

Table 5 Jet penetration and bandwidth at $x/d_j = 8$

Case	Penetration height	Penetration bandwidth
Gruber et al. [3]	$3.1d_j$	——
Rothstein and Wantuck [27]	$4.3d_j$	——
Ben-Yakar et al. [2]	$5.3d_j$	$2.7d_j$
Present simulation	$4.3d_j$	$1.4d_j$

heights of $3.1d_j$, $4.3d_j$, $5.3d_j$, and $4.3d_j$ correspond to Gruber et al. [3], Rothstein and Wantuck [27], Ben-Yakar et al. [2], and the present simulation, respectively. These discrepancies between experiments might to be due to the experiment-dependent measuring techniques and criterion. The jet penetration, as measured in Gruber et al.'s Mie scattering [3], corresponds to 10% of the jet concentration, whereas Ben-Yakar et al.'s [2] results correspond to 1% of the same. Therefore, the penetration measurements based on Mie scattering are somewhat lower than the ones based on 1%-concentration measurements. Although OH fluorescence is used to visualize jet penetration, better agreement with Ben-Yakar et al.'s results is achieved through the correlation of Rothstein and Wantuck [27]. The relatively good agreement seems to be the result of experimental similarities.

The discrepancies between the experimental and numerical results, regarding the jet penetration and bandwidth, probably stem from ambiguities in the boundary conditions, such as the properties of steady incoming flow and fixed jet-exit conditions. For injection experiments in impulse facilities, the incoming and injector boundary layers contain turbulent structures with characteristic length scales. However, the present simulation uses steady inflow conditions at the injector exit and inflow boundary. These assumptions cause a lack of turbulent intensities in the boundary layer and jet flow around the injector exit, which results in lower jet penetration and a narrower jet bandwidth.

Table 5 summarizes the jet penetration and bandwidth data at $8d_j$ downstream of the injection port. Although there are some differences between the results from the experiments and the simulations, the simulation results follow the experimental trends well, and the resulting values are thought to be reasonable.

IV. Results and Discussion

A. Temporal Evolution of Large Coherent Structures

The most interesting features of a transverse jet in crossflow are the large-scale coherent structures and their time-dependent evolution, which are easily identified in consecutive instantaneous images. As the jet-shear-layer vortices travel downstream, they interact with the freestream and play important roles in the near-field mixing process. An analysis of temporal evolution using time-correlated images gives further insight into the coherence and mixing properties of the injection flowfield.

The consecutive schlieren images, as shown in Fig. 6, are obtained from an ultrahigh-speed schlieren system in the experiment. The exposure time of each image is 100 ns, and the interframing time is 1 μs. The equivalent overlaid hydrogen mass fraction and pressure contour images are extracted from the numerical results and included in Fig. 6. In both the experimental and numerical images, large-scale eddies are periodically generated at the early stages of the jet–freestream interaction and bend with the crossflow. In the region of bending, the velocity gradient between the high-speed freestream and the low-speed jet flow leads to the stretching of the large-eddy structures. This stretching process also enlarges the eddy structures and causes the freestream to be engulfed by the jet shear layer. As the eddy velocity approaches the freestream velocity, the stretching process becomes constant beyond three or four jet diameters downstream.

The consecutive overlaid images of the pressure and hydrogen mass fraction also demonstrate the fluctuating bow shock well. The attached bow shock structure depends strongly on the large-scale eddy structures, especially in the vicinity of the jet exit. Conversely, this fluctuating bow shock may affect the eddy stretching and near-field mixing process by inducing variation in the velocity around the large- eddy structures. However, the effects of the fluctuating shock seem to be minor, because the fluctuation is restricted to the vicinity of the jet exit.

A direct comparison of each temporal eddy position is carried out to assess the numerical results on the convection characteristics and eddy-formation frequency for the unsteady transverse injection flowfield. The predicted temporal positions of eddy 1 agree well with the experimental results. However, for other eddy positions, there are some differences between the results from the experiments and those from the simulations. The eddy-formation frequency under the simulation is also slightly different from the corresponding

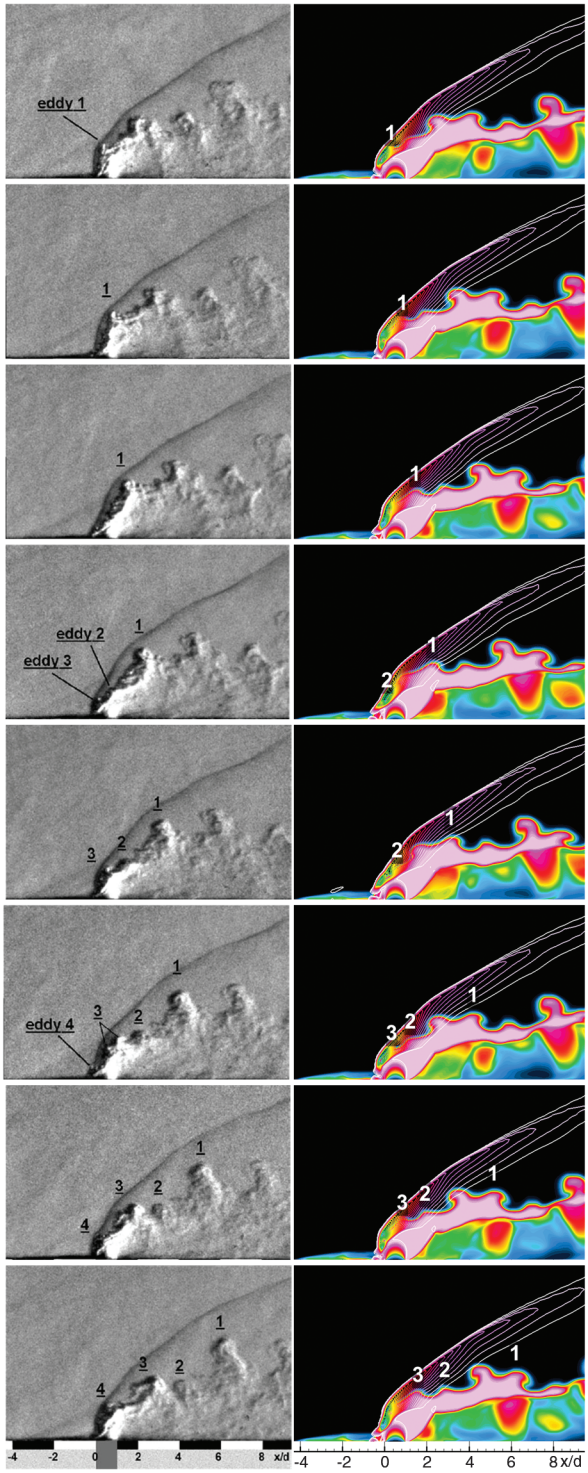

Fig. 6 Consecutive schlieren images [2] and equivalent overlaid simulation images of the hydrogen mass fraction and pressure contours with an interframing time of 1 μs.

experimental results. In the simulation, four eddies are formed over a duration of 10 μs, whereas in the experiment, four eddies are formed over an even shorter duration of 7 μs.

For quantitative comparison, the centroid trajectories of the identifiable coherent structures have been traced in the space-time domain. Again, Fig. 7 shows a good coincidence for eddy no. 1. The temporal positions of eddy 3 in the numerical results agree well with those of eddy 2 in the experimental results. This means that the present simulation is capable of capturing the convection velocities of large-scale eddies but is relatively inadequate for resolving the eddy-formation frequency. The eddy-formation position and frequency in the experimental results are relatively irregular, whereas the numerical results show a regular pattern. In numerical simulation, all eddies are formed at about $0.3d_j$, and the even- and odd-numbered eddies (i.e., eddies 1 and 3 and eddies 2 and 4) show very similar convection characteristics. These regular patterns can be confirmed in the pressure-time history at the wall, as shown in Fig. 8. The pressure-time history, including the time horizon of Fig. 7, shows very regular patterns, and these clarify the previous periodic eddy-formation characteristics. The comparison between the pressure-time history and eddy-formation frequency also reveals that two eddies are generated during one cycle of the pressure-time history. This implies that eddies 1 and 3 and eddies 2 and 4 are basically the same.

The difference between the numerical and experimental results in the eddy-formation frequency seems to arise from the deficiency of the turbulence model and some ambiguities in boundary conditions. The large-scale eddies are generated close to the attached boundary layer in the vicinity of the jet exit, where the RANS mode is activated in the current DES approach. The RANS mode attempts to model all scales of turbulence and, therefore, cannot resolve the energy containing eddies in the boundary layer. Small mismatches in the boundary conditions in numerical simulation (in the course of the attempt to dictate experimental conditions, such as uniform incoming flow and fixed jet-exit properties) may affect the unsteady flowfield around the injector exit. Therefore, these limitations of the turbulence model and boundary conditions may change the Kelvin–Helmholtz instability, which determines the eddy-formation frequency.

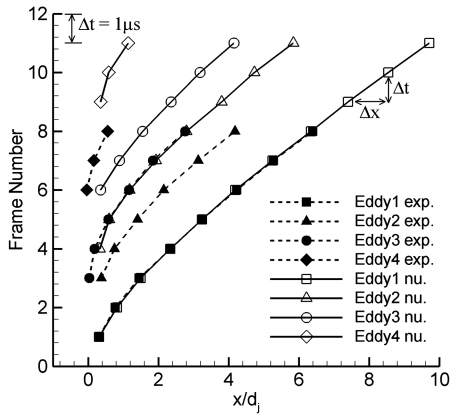

Fig. 7 Space-time trajectories of large-scale eddies.

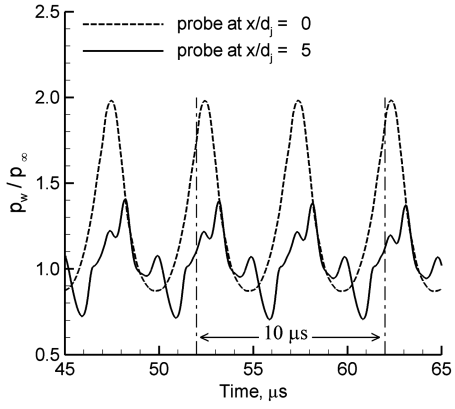

Fig. 8 Pressure-time histories at the bottom wall.

B. Mechanism of Formation of Large Coherent Structures

In the previous subsection, we examined the temporal behavior of coherent structures and found that the jet vortical structure was one of the primary controlling parameters for near-field mixing. Therefore, we expect to improve the understanding of mixing characteristics if we know the mechanism of formation of these structures. The origin of the jet vortical structures has been studied by several researchers. Kelso et al. [28] observed the formation of vortex rings around the jet periphery in their low Reynolds-number experiments. Yuan et al. [29] performed a LES of transverse jets in subsonic crossflows and found two kinds of vortices: spanwise rollers and hanging vortices. Kawai and Lele [10] tried to investigate the mixing mechanism in a supersonic flowfield, using a LES. They discussed the interaction between the vortices inside the recirculation region and the jet shear layer; their results might be a precursor of the results presented next.

Figure 9 shows the vorticity field around the jet exit. The vorticity magnitude of ω_m is mainly distributed fore and aft of the jet and along the jet shear layer, as shown in Fig. 9a. The vorticity magnitude consists of three vortical components (i.e., ω_x, ω_y, and ω_z); hence, it is necessary to examine the contribution of each vortical component to the vorticity magnitude. By comparing the vorticity magnitude and each vortical component, as shown in Figs. 9b–9d, we know that the major contribution to the vorticity magnitude is made by ω_y. Although ω_x and ω_z have only minor effects on the jet downstream, the overall vorticity field is very similar between ω_y and ω_m, except that the contour color is different because of the ω_y sign, according to the rotational direction.

On the basis of this correlation, the temporal evolution of ω_y around the jet exit is illustrated in Fig. 10. The interaction between the vortices inside the upstream recirculation region and the jet shear layer induces the unsteady shock fluctuation and accompanies the jet vortical structures. In the region that is immediately upstream of the jet, two counter-rotating vortices, one positive and the other negative, are detached alternately. When the outward positive vorticity is detached at $\Delta t = 1$ μs, the first eddy is formed. The detached vorticity passes through the jet shear layer and simultaneously impacts the bow shock structure, while changing its local shape. The second eddy is generated as the inward negative vorticity is detached at $\Delta t = 4$ μs. The inward vorticity, as it also goes through the jet shear layer, blocks the supersonic jet and deforms the barrel shock structure. This chain of events is repeated periodically with a period of about 5 μs; therefore, the third and fourth eddies are generated in a similar manner, as shown in the series of images. These procedures can be compared with the previous temporal evolutions of eddy structures for explaining the numerical eddy-formation frequency.

The previous vorticity analysis provides some insights into the velocity gradient effects on the mixing properties and eddy-forming processes. The strong vortical structures that originate from kinematic velocity gradients are distributed around the jet exit and along the jet shear layer, as described in Fig. 9. The velocity gradients between the crossflow behind the bow shock and the jet affect the tilting and stretching of eddies, while contributing to the mixing process. These phenomena are also observed downstream of the Mach disk, where the jet flow across the Mach disk becomes subsonic and the crossflow remains almost unchanged across the weak bow shock. Close to the jet exit, the two counter-rotating vortices are detached alternately and generate the corresponding eddies, as shown in Fig. 10. In these eddy-forming processes, the positive vorticity (also known as the primary upstream vorticity) seems to be related to the freestream velocity and the negative vorticity (also known as the secondary upstream vorticity) may scale with the jet-exit velocity. These velocity gradient effects on the mixing properties and eddy-formation frequency are also observed in

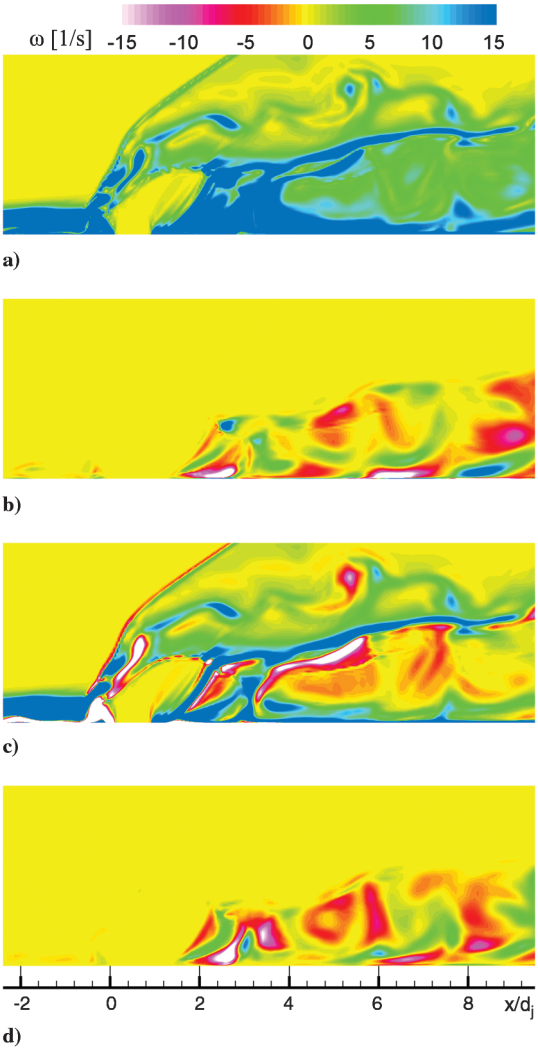

Fig. 9 Vorticity distribution around the jet exit: a) magnitude of the vorticity ω_m, b) x component of the vorticity ω_x, c) y component of the vorticity ω_y, and d) z component of the vorticity ω_z.

Ben-Yakar et al.'s [2] experiment; the present numerical results can supplement their experimental achievements.

C. Ignition of a Hydrogen Transverse Jet

The ignition and flame stabilization of a transverse jet that is injected into high-enthalpy supersonic crossflows are problematic issues because of the limited flow residence time and high strain rate. The short residence time induces greater dependence of the ignition delay time (and therefore combustion) and the high strain rate tends to suppress combustion in compressible supersonic flowfields. This subsection investigates the near-field self-ignition of a hydrogen transverse jet that is injected into supersonic crossflow.

For self-ignition to be accomplished in a supersonic combustible mixture, it is necessary that four quantities have suitable values [30]: the static temperature, the static pressure, the equivalence ratio, and the residence time. As a conventional scheme in supersonic combustors, transverse injection provides two main ignition points where ignition is likely to occur: the recirculation region ahead of the jet where long residence times and high temperatures exist and the region behind the jet bow shock where high temperatures and pressures prevail.

Figure 11 presents instantaneous experimental and numerical images of the OH distribution at the centerline. The OH radical is an intermediate species that appears during hydrogen combustion and its gradient is generally assumed to correspond to the flame-front location. OH–PLIF provides a two-dimensional visualization that maps the self-ignition locations. Figure 11a is an experimental OH–

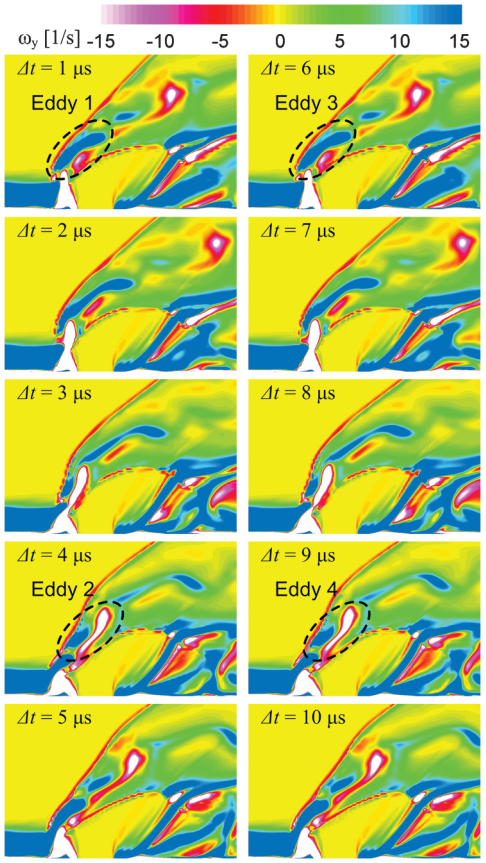

Fig. 10 Temporal evolution of ω_y in the vicinity of the jet exit.

PLIF image and demonstrates a continuous and thin OH filament along the jet-shear-layer periphery. The OH radicals are produced primarily behind the steep bow shock, as well as in the recirculation region upstream of the jet exit, and transported downstream with the shear layer vortices. However, further downstream, a decrease in the OH signal is observed as the mixture expands around the jet flowfield. The invisible OH signal at the center of the jet plume also

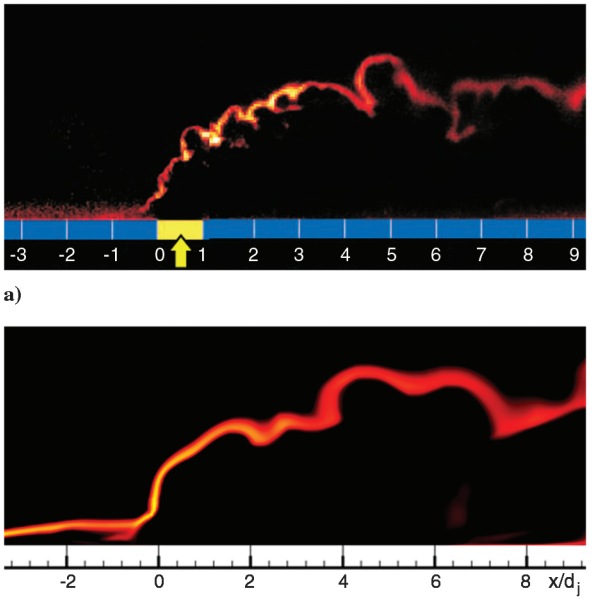

Fig. 11 Experimental OH–PLIF [30] and the corresponding numerical OH distribution at the center plane of the jet: a) experimental OH–PLIF and b) numerical OH distribution.

indicates poor mixing of the air with the core of the hydrogen jet. The numerical OH distribution, as shown in Fig. 11b, is capable of describing the previously mentioned combustion characteristics.

A relatively cold hydrogen jet is injected into hot freestream air in Ben-Yakar's experiment [30], and there will be a significant temperature variation with the equivalence ratio (φ) through the mixing layer around the jet. The ignition delay time is a strong function of the mixture temperature and the mixture temperature will be higher at low equivalence ratios. Therefore, self-ignition is expected to occur on the fuel-lean side of the mixing layer around the jet ($\varphi \approx 0.2$) [30].

Ben-Yakar [30] tried to estimate the characteristic time scales of the ignition process to explain their OH–PLIF results. They measured the bow shock angle from the long-exposure schlieren image and applied oblique shock wave theory to calculate the static temperature ($T_{2,\text{exp.}}$) and pressure ($p_{2,\text{exp.}}$) of the freestream behind the bow shock wave. They assumed the hydrogen temperature (T_{H2}) to be 300 K, which is slightly different from the experimental hydrogen temperature of 246 K. To approximate the mixture temperature ($T_{\text{mix,exp.}}$) at $\varphi = 0.2$, a simplified one-dimensional enthalpy-balance equation was used between the cold hydrogen of T_{H2} and the hot freestream of $T_{2,\text{exp.}}$. However, the mixture pressure ($p_{\text{mix,exp.}}$) at $\varphi = 0.2$ was taken as the value of $p_{2,\text{exp.}}$ due to the lack of a theoretical method to describe the pressure variation behind the bow shock wave. Based on $T_{\text{mix,exp.}}$ and $p_{\text{mix,exp.}}$ at $\varphi = 0.2$, the ignition delay times ($\tau_{\text{exp.}}$) were calculated at several locations along the x axis; the results are summarized in Fig. 12a. A similar procedure was conducted for the numerical estimation of the ignition delay time ($\tau_{\text{nu.}}$); the numerically calculated values are compared with the experimentally calculated results in Fig. 12a.

The experimentally calculated results shown in Fig. 12a indicate that instantaneous self-ignition is achieved close to the jet exit as the ignition delay times are of the order of 1–2 μs. Further downstream, beyond $x/d_j = 6$, the ignition delay times become longer ($\tau_{\text{exp.}} > 10$ μs) and exceed the maximum flow residence time of the imaged region ($\approx 10 d_j$). However, the numerically calculated ignition delay times are over twice the experimentally calculated results. For example, at the location of $x/d_j = 6$, the experimentally calculated ignition delay time, $\tau_{\text{exp.}}$, is 10 μs, whereas the numerically calculated ignition delay time, $\tau_{\text{nu.}}$, is 37 μs. Although there is some disparity between the experimental and numerical estimations, we can conclude that the OH radicals are generated only near the jet exit and transported downstream with the shear layer vortices. Because new radicals are not produced far downstream of the injector, the OH concentration decreases; therefore, the OH–PLIF signal is reduced.

The disparity in the ignition delay times may be attributed to the restricted availability of both numerical and experimental data. In the case of the experiment, the static properties, $T_{2,\text{exp.}}$ and $p_{2,\text{exp.}}$, behind the bow shock wave and the mixture temperature $T_{\text{mix,exp.}}$ at $\varphi = 0.2$ are reasonable, but the mixture pressure $p_{\text{mix,exp.}}$ at $\varphi = 0.2$ is overpredicted due to the previously mentioned reason. The effect of the assumed hydrogen temperature is minor, because $T_{\text{mix,exp.}}$ is determined on the fuel-lean side of the mixing layer. Therefore, the experimentally calculated ignition delay time $\tau_{\text{exp.}}$ may be shorter than the exact value. On the other hand, in the present simulation, the mixture properties, $T_{\text{mix,nu.}}$ and $p_{\text{mix,nu.}}$, at $\varphi = 0.2$, as well as the static properties, $T_{2,\text{nu.}}$ and $p_{2,\text{nu.}}$, behind the bow shock wave, can be extracted from the numerical results. However, because the bow shock angle predicted by numerical simulation is slightly lower than that of the experiment (see the inset of Fig. 12b), the overall flow properties are slightly underpredicted. Therefore, the numerically calculated ignition delay time $\tau_{\text{nu.}}$ may be longer than the exact value. Figure 12b clearly shows the differences between the experimental and numerical flow properties along the vertical dashed line in Fig. 12a at $x/d_j = 6$. The relatively small difference between $T_{\text{mix,exp.}}$ and $T_{\text{mix,nu.}}$ at $\varphi = 0.2$ cannot be ignored due to its exponential effect on the ignition delay time. The large difference between $p_{\text{mix,exp.}}$ and $p_{\text{mix,nu.}}$ at $\varphi = 0.2$ also causes a disparity in the ignition delay time because of the two-body reactions that are involved in the ignition chemistry of hydrogen and air. The specific property values used in the calculation of the ignition delay time at $x/d_j = 6$ are summarized in Table 6.

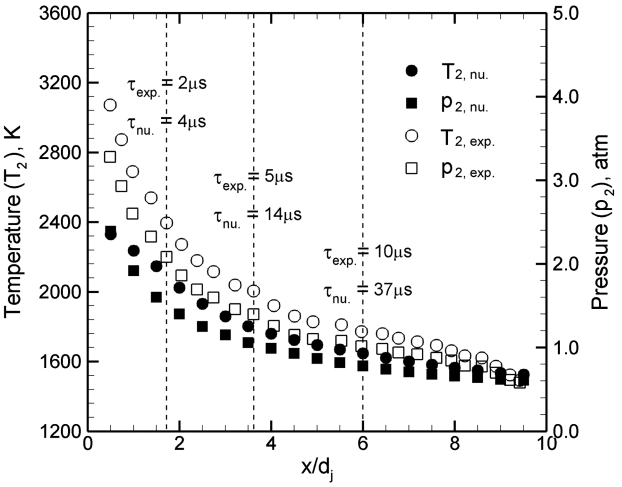

a)

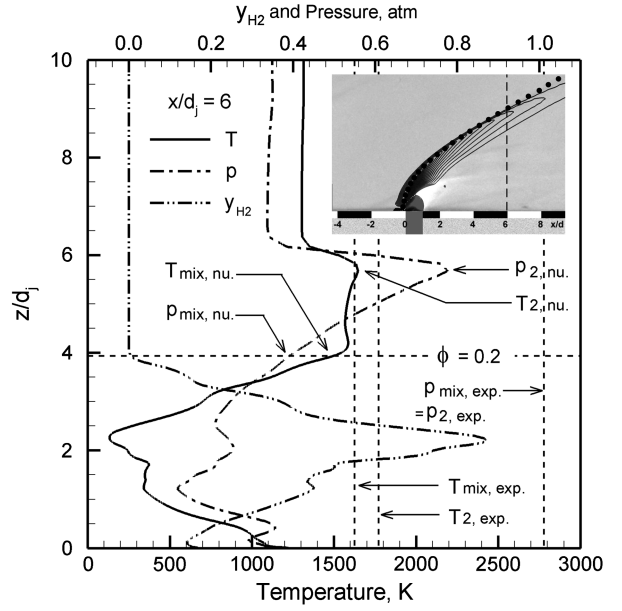

b)

Fig. 12 Comparison of the experimental [30] and numerical ignition delay times: a) ignition delay times at several locations and b) experimental measurements and numerical values of the flow properties at $x/d_j = 6$.

D. Effects of the Turbulence Model on Combustion

The present subsection investigates the effects of the turbulence model on the near-field combustion characteristics. To identify the

Table 6 Experimental [30] and numerical flow properties along the vertical dashed line at $x/d_j = 6$ (Fig. 12b)

Property	Ben-Yakar experiment [30]	Present simulation
	Behind the bow shock ($x/d_j = 6$)	
T_2, K	1771	1646
p_2,. atm	1.01	0.78
T_{H2}, K	300	246
	Mixing layer of $\varphi = 0.2$ ($x/d_j = 6$)	
T_{mix}, K	1624	1501
p_{mix}, atm	1.01	0.39
τ, μs	10	37

effects of changing the turbulence model, the DES results are compared with those of RANS in terms of the H_2O mass flux distributions. This is because H_2O is the primary species of hydrogen combustion and can be considered an indicator for the amount of combustion and the reaction zone.

Figure 13 shows the H_2O mass flux distributions for the RANS and DES approaches. In the case of the RANS turbulence model, a smooth and diffusive reaction zone is observed along the outer edge of the jet, as shown in the side view (i.e., the x–z plane) image of Fig. 13a. The consecutive end-view (i.e., the y–z plane) images illustrate that the elongated reaction band increases with the downstream distance. However, the reaction zone is not observed in the jet core. On the other hand, the DES approach in Fig. 13b yields the unsteady fluctuating distributions. The transverse and lateral fluctuations due to large-scale eddy motions are clearly apparent in the instantaneous side- and end-view images. Unlike the case with the RANS computations, a partial reaction zone is also observed in the jet core and penetrates further downstream. Finally, the time-averaged DES results are shown in Fig. 13c. The broad reaction zone looks similar to that under RANS, but the underlying mechanism is completely different. Although the diffusive reaction zone of RANS is due to its intrinsic dissipative characteristics, the broad reaction zone of DES can be explained by the intermittency effects. As shown in Fig. 13b, the reaction zone is wrinkled and displaced by the large-scale eddy motions and the extreme positions that are attained by the instantaneous reaction zone determine the average reaction-zone thickness at a given location.

For a quantitative comparison, the mass flow rates of H_2O along the x-axial cross section are examined and compared in Fig. 14. Because of the unavailability of experimental data, the key point here is the differences between the simulations, not the absolute values of the predicted quantities. The instantaneous mass flow rates are extracted from the discrete DES results with an interval of 1 μs and they are well represented in the time-averaged value, which is located in the middle of the fluctuating band. Compared with the time-averaged DES value, the RANS calculation reveals an increase of roughly 40% in the mass flow rate of H_2O at $x/d_j = 10$. This is surprising, given that the enhanced mixing causes more combustion.

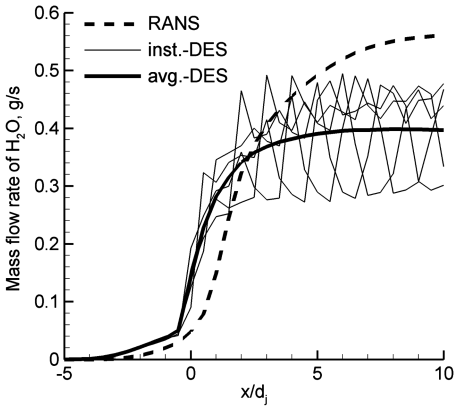

Fig. 14 Mass flow rate of H_2O along the x-axial cross section.

In a DES flowfield, unlike the case of a steady RANS flowfield, mixing is enhanced by the resolved large-scale eddy motions; therefore, combustion is also expected to be enhanced.

An interesting difference is found in the distribution of the turbulent viscosity shown in Fig. 15. This may hold a clue to the earlier unexpected result. Although large values of the turbulent viscosity are observed only along the bow and barrel shocks in the DES, a completely different distribution is yielded by the RANS simulation. Extremely large values of the turbulent viscosity are distributed over most of the jet shear layer. This is natural, because the RANS approach is not expected to capture the unsteadiness. However, there is a noticeable difference in the magnitudes of the turbulent viscosity, which in the RANS case are approximately four times more than those under the DES predictions. This large turbulent viscosity causes a large turbulent mass diffusivity due to the assumed constant Schmidt number, which is defined as the ratio of the viscous diffusion rate to the mass diffusion rate. Therefore, the greater amount of combustion in the RANS calculation can be explained by this large turbulent mass diffusivity.

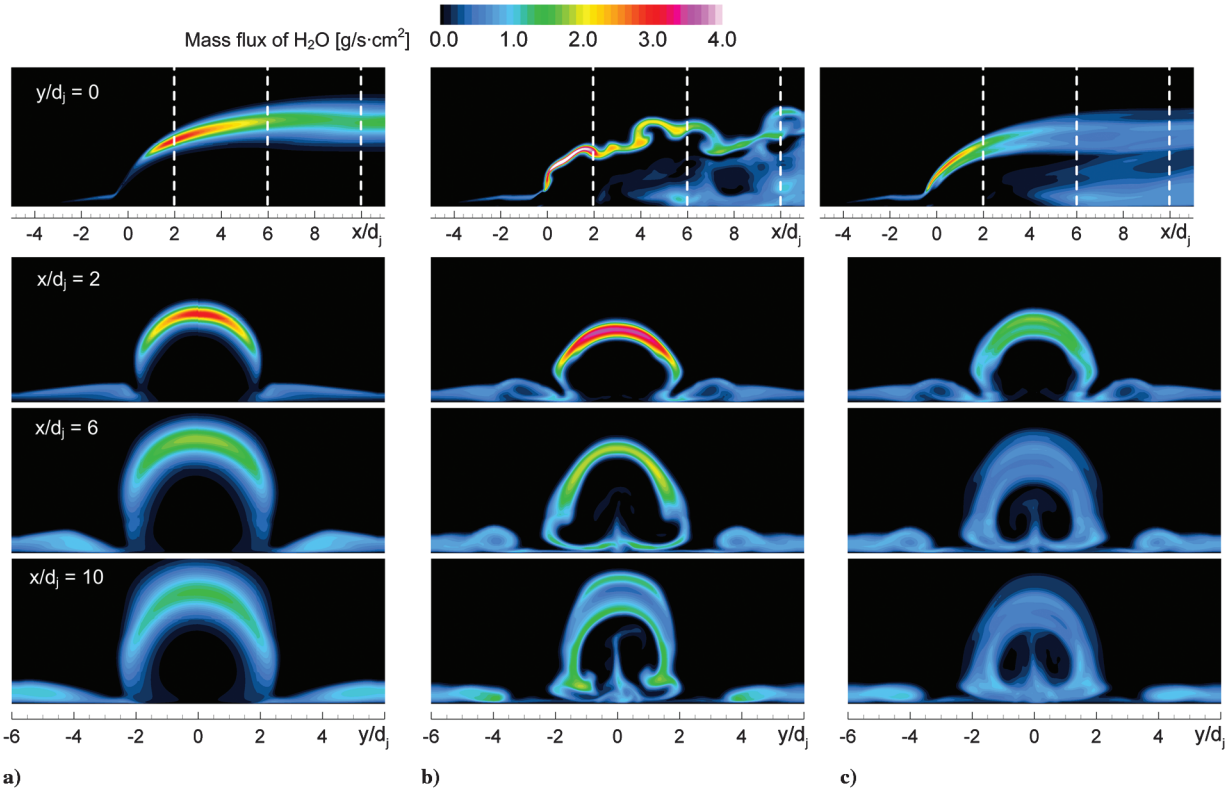

Fig. 13 Spatial distribution of the H_2O mass flux: a) RANS, b) instantaneous DES, and c) time-averaged DES.

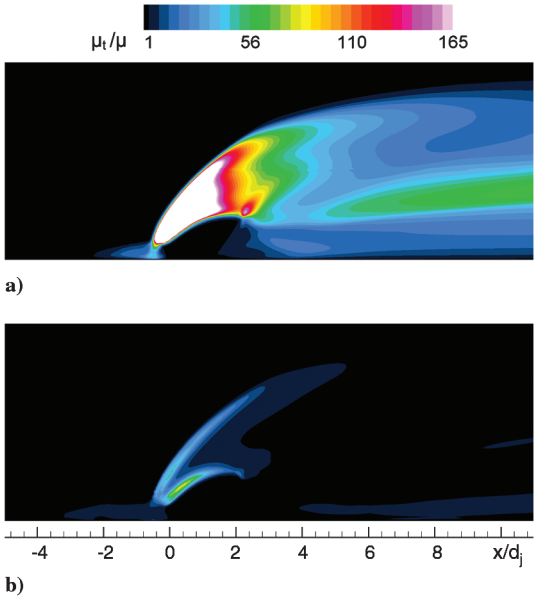

Fig. 15 Turbulent viscosity distribution around the jet exit: a) RANS and b) time-averaged DES.

As the large-scale eddy structures and related intermittency phenomena are explicitly resolved at a given time and space, the current DES approach seems to provide a more reliable description of the turbulent reacting flowfield. For a given amount of combustion, the RANS estimate exceeds that of the DES estimate due to the large turbulent mass diffusivity, although the latter fails to capture the features of unsteady turbulent flow. Therefore, it can be considered that the RANS turbulence model significantly overpredicts the near-field combustion characteristics of the transverse jet in crossflow.

V. Conclusions

We have numerically investigated the turbulent mixing and reacting flow physics for the transverse jet in crossflow in a real supersonic combustor environment. Comprehensive numerical simulations were performed using DES and a finite-rate chemistry model. For verification purposes, grid refinement with the GCI concept was introduced for the instantaneous flowfield. The considered grid system was sufficient to resolve unsteady turbulent flow characteristics and the resultant GCI based on the temporal pressure history indicated that the solutions were well within the asymptotic range of convergence. For validation purposes, comparisons were made with quantitative experimental measurements. Although the numerically predicted results yielded slightly lower jet penetrations and narrower jet bandwidths, the overall comparison showed good agreement of the numerical results with experimental trends.

The temporal evolution using the space-time trajectories of large-scale eddies has revealed that the numerical flowfield replicates well the experimental convective characteristics. However, a slight overprediction is observed with regard to the eddy-formation frequency. The difference between the numerical and experimental results is attributable to the deficiency of the RANS turbulence model, which is activated in the attached boundary layer in the vicinity of the jet exit, where the large-scale eddies are generated. These incomplete turbulence properties may influence the Kelvin–Helmholtz instability, which controls the eddy-formation frequency. The temporal vorticity analysis reveals the mechanism of formation of the jet vortical structures. As the interacting counter-rotating vortices are detached alternately from the upstream recirculation region, the corresponding eddies are generated and this chain of events is repeated periodically. This mechanism of vorticity generation provides some clues to the velocity gradient effects on the mixing properties and eddy-formation frequency, which are observed in Ben-Yakar et al.'s experiment [2].

For the turbulent reacting flowfield, the numerical OH distribution describes the experimental OH–PLIF image very well, which maps the locations of self-ignition. Further quantitative comparison reveals that the numerically estimated ignition delay times are over twice those of the experimental results. This disparity can be attributed to the inadequacy of the available experimental and numerical data for calculating the exact ignition delay time. However, both the experimental and numerical results show that the OH radicals are generated only near the jet exit and diluted as they are transported downstream. Through a comparative analysis of the results of the RANS and DES approaches, the effects of the turbulence model on combustion are examined. As expected, the intermittency phenomena are observed only in the DES calculation. However, a greater amount of combustion occurs in the RANS calculation. This is mainly due to the excessive turbulent mass diffusivity. As the intermittent eddy motions are explicitly resolved, the DES approach is supposed to describe a reliable turbulent reacting flowfield. This capability of capturing the intermittency characteristics is a significant advantage of DES compared with RANS and must be incorporated in the simulation of reacting flowfields to take into account the probability of reaction at a given location.

Acknowledgments

The present study was supported by the basic research grants of the Defense Acquisition Program Administration, through the Agency for Defense Development, and the National Research Foundation of Korea grant, funded by the Korean Government (Ministry of Education, Science, and Technology). The authors would like to thank Ronald K. Hanson of Stanford University and Adela Ben-Yakar of the University of Texas at Austin for providing experimental data and for informed discussions regarding this topic.

References

[1] Fric, T. F., and Roshko, A., "Vortical Structure in the Wake of a Transverse Jet," *Journal of Fluid Mechanics*, Vol. 279, 1994, pp. 1–47. doi:10.1017/S0022112094003800

[2] Ben-Yakar, A., Mungal, M. G., and Hanson, R. K., "Time Evolution and Mixing Characteristics of Hydrogen and Ethylene Transverse Jets in Supersonic Crossflows," *Physics of Fluids*, Vol. 18, No. 2, 2006, Paper 026101. doi:10.1063/1.2139684

[3] Gruber, M. R., Nejad, A. S., Chen, T. H., and Dutton, J. C., "Mixing and Penetration Studies of Sonic Jets in a Mach 2 Freestream," *Journal of Propulsion and Power*, Vol. 11, No. 2, 1995, pp. 315–323. doi:10.2514/3.51427

[4] Gruber, M. R., Nejad, A. S., Chen, T. H., and Dutton, J. C., "Bow Shock/Jet Interaction in Compressible Transverse Injection Flowfields," *AIAA Journal*, Vol. 34, No. 10, 1996, pp. 2191–2193. doi:10.2514/3.13372

[5] Papamoschou, D., and Hubbard, D. G., "Visual Observations of Supersonic Transverse Jets," *Experiments in Fluids*, Vol. 14, No. 6, 1993, pp. 468–471. doi:10.1007/BF00190201

[6] Tam, C.-J., Baurle, R. A., and Gruber, M. R., "Numerical Study of Jet Injection into a Supersonic Crossflow," AIAA Paper 1999-2254, 1999.

[7] Palekar, A., Truman, C. R., and Vorobieff, P., "Prediction of Transverse Injection of a Sonic Jet in Supersonic Crossflow," AIAA Paper 2005-5366, 2005.

[8] Peterson, D. M., Subbareddy, P. K., and Candler, G. V., "DES Investigation of Transverse Injection into Supersonic Crossflow Using a Hybrid Unstructured Solver," AIAA Paper 2006-903, 2006.

[9] Peterson, D. M., Subbareddy, P. K., and Candler, G. V., "Assessment of Synthetic Inflow Generation for Simulating Injection Into a Supersonic Crossflow," AIAA Paper 2006-8128, 2006.

[10] Kawai, S., and Lele, S. K., "Mechanisms of Jet Mixing in a Supersonic Crossflow: A Study Using Large-Eddy Simulation," AIAA Paper 2008-4575, 2008.

[11] Boles, J. A., Edwards, J. R., and Baurle, R. A., "Hybrid LES/RANS Simulation of Transverse Sonic Injection into a Mach 2 Flow," AIAA Paper 2008-622, 2008.

[12] Choi, J.-Y., Yang, V., and Ma., F., "Combustion Oscillations in a Scramjet Engine Combustor with Transverse Fuel Injection," *Proceedings of the Combustion Institute*, Vol. 30, No. 2, 2005,

pp. 2851–2858.
doi:10.1016/j.proci.2004.08.250
[13] Choi, J.-Y., Ma, F., and Yang, V., "Dynamics Combustion Characteristics in Scramjet Combustors with Transverse Fuel Injection," AIAA Paper 2005-4428, 2005.
[14] von Lavante, E., Zeitz, D., and Kallenberg, M., "Numerical Simulation of Supersonic Airflow with Transverse Hydrogen Injection," *Journal of Propulsion and Power*, Vol. 17, No. 6, 2001, pp. 1319–1326.
doi:10.2514/2.5881
[15] Won, S.-H., Jeung, I.-S., Shin, J.-R., Cho, D.-R., and Choi, J.-Y., "Three-Dimensional Dynamic Characteristics of Transverse Fuel Injection into a Supersonic Crossflow," AIAA Paper 2008-2515, 2008.
[16] Choi, J.-Y., Jeung, I.-S., and Yoon, Y., "Computational Fluid Dynamics Algorithms for Unsteady Shock-Induced Combustion, Part 1: Validation," *AIAA Journal*, Vol. 38, No. 7, 2000, pp. 1179–1187.
doi:10.2514/2.1112
[17] Spalart, P. R., Jou, W.-H., Strelets, M., and Allmaras, S. R., "Comments on the Feasibility of LES for Wings, and on a Hybrid RANS/LES Approach," *Advances in DNS/LES: 1st AFOSR International Conference on DNS/LES*, Columbus, OH, 1997, pp. 137–148.
[18] Strelets, M., "Detached Eddy Simulation of Massively Separated Flows," AIAA Paper 2001-0879, 2001.
[19] Menter, F. R., "Two-Equation Eddy-Viscosity Turbulence Models for Engineering Applications," *AIAA Journal*, Vol. 32, No. 8, 1994, pp. 1598–1605.
doi:10.2514/3.12149
[20] Peters, N., "Multiscale Combustion and Turbulence," *Proceedings of the Combustion Institute*, Vol. 32, No. 1, 2009, pp. 1–25.
doi:10.1016/j.proci.2008.07.044
[21] Möbus, M., Gerlinger, P., and Brüggemann, D., "Scalar and Joint Scalar-Velocity-Frequency Monte Carlo PDF Simulation of Supersonic Combustion," *Combustion and Flame*, Vol. 132, Nos. 1–2, 2003, pp. 3–24.
doi:10.1016/S0010-2180(02)00428-5
[22] Norris, J. W., and Edwards, J. R., "Large-Eddy Simulation of High-Speed Turbulent Diffusion Flames with Detailed Chemistry," AIAA Paper 1997-0370, 1997.
[23] Fureby, C., "Comparison of Flamelet and Finite Rate Chemistry LES for Premixed Turbulent Combustion," AIAA Paper 2007-1413, 2007.
[24] Smith, G. P., Golden, D. M., Frenklach, M., Moriarty, N. W., Eiteneer, B., Goldenberg, M., Bowman, C. T., Hanson, R. K., Song, S., Gardiner, W. C., Jr., Lissianski, V. V., and Qin, Z., "GRI-Mech 3.0" [online database], http://www.me.berkeley.edu/gri_mech/ [retrieved 22 Sept. 2008].
[25] Roache, P. J., "Error Bars for CFD," AIAA Paper 2003-0408, 2003.
[26] Roache, P. J., "Verification of Code and Calculations," *AIAA Journal*, Vol. 36, No. 5, 1998, pp. 696–702.
doi:10.2514/2.457
[27] Rothstein, A. D., and Wantuck, P. J., "A Study of the Normal Injection of Hydrogen Into a Heated Supersonic Flow Using Planar Laser-Induced Fluorescence," AIAA Paper 1992-3423, 1992.
[28] Kelso, R. M., Lim, T. T., and Perry, A. E., "An Experimental Study of Round Jets in Cross-Flow," *Journal of Fluid Mechanics*, Vol. 306, 1996, pp. 111–144.
doi:10.1017/S0022112096001255
[29] Yuan, L. L., Street, R. L., and Ferziger, J. H., "Large-Eddy Simulation of a Round Jet in Crossflow," *Journal of Fluid Mechanics*, Vol. 379, 1999, pp. 71–104.
doi:10.1017/S0022112098003346
[30] Ben-Yakar, A., "Experimental Investigation of Mixing and Ignition of Transverse Jets in Supersonic Crossflows," Ph.D. Dissertation, Mechanical Engineering Dept., Stanford Univ., Stanford, CA, 2000.

J. Sahu
Associate Editor